

Winding number dependence of Bose-Einstein condensates in a ring-shaped lattice

D. M. Jezek and H. M. Cataldo

IFIBA-CONICET

and

Departamento de Física,

FCEN-UBA Pabellón 1,

Ciudad Universitaria,

1428 Buenos Aires, Argentina

(Dated: February 16, 2022)

Abstract

We study the winding number dependence of the stationary states of a Bose-Einstein condensate in a ring-shaped lattice. The system is obtained by confining atoms in a toroidal trap with equally spaced radial barriers. We calculate the energy and angular momentum as functions of the winding number and the barrier height for two quite distinct particle numbers. In both cases we observe two clearly differentiated regimes. For low barriers, metastable vortex states are obtained up to a maximum winding number which depends on the particle number and barrier height. In this regime, the angular momentum and energy show, respectively, almost linear and quadratic dependences on the winding number. For large barrier heights, on the other hand, stationary states are obtained up to a maximum winding number which depends only on the number of lattice sites, whereas energy and angular momentum are shown to be sinusoidal functions of the winding number.

PACS numbers: 03.75.Lm, 03.75.Hh, 03.75.Kk

I. INTRODUCTION

Ultra-cold atoms in optical lattices nowadays represent a perfect laboratory system for the quantitative study of various condensed-matter models. In addition to offering an extremely high degree of experimental control and reproducibility, such systems have shown to provide a very useful theoretical testing ground for the quantum modeling of strongly correlated many-body systems. Perhaps the most simple and fecund of such applications is given by the dynamics of double-well Bose-Einstein condensates [1], which has been extensively studied in recent years [2]. In particular, for high enough barriers, a simple two-mode model Hamiltonian describing Josephson-oscillations and quantum self-trapping phenomena, has been analyzed by different authors [3–6], and later improved to better introduce interparticle interaction effects [7]. On the other hand, the associated dynamics has been experimentally observed a few years ago [8].

In the last years, this research work has been extended to multiple well condensates motivated by the possibility of generating and manipulating vortex states. In a recent experiment, Scherer *et al.* [9] have reported observations of vortex formation by merging and interfering multiple Bose-Einstein condensates in a confining potential. In their experiment, a single harmonic potential well was partitioned into three sections by barriers forming three independent Bose-Einstein condensates, which had no coherence between the respective phases. By removing the barriers, the condensates merged together and it has been shown that, depending on the unknown initial relative phases, the final state could acquire vorticity. The authors have observed single vortex states even after five seconds following the barrier ramp-down, indicating relatively long single vortex lifetimes. This experiment stimulated theoretical investigation as regards the maximum winding number a condensate in a ring-shaped lattice could sustain, depending on the trap properties, particularly, on the barrier height between wells. For example, in the case of large barrier heights, the problem of vortex trapping in cyclically coupled Bose-Josephson junctions has been recently addressed by Ghosh and Sols [10]. They coupled initially independent Bose-Einstein condensates through Josephson links and allowed the system to reach a stable circulation by adding a dissipative term in semiclassical equations of motion. In addition, the authors analyzed the probability of trapping a vortex with a given winding number, finding that a necessary condition to obtain a metastable nonzero circulation consists of generating a winding number smaller

than a quarter of the total number of linked condensates. A different approach was utilized by Pérez-García *et al.* [11], which by means of group-theoretical methods, studied charge inversion and vortex erasing in condensates confined by traps with discrete symmetries [12]. They have predicted the existence of stationary states up to a winding number which depends on the order of the symmetry. On the other hand, the case of a continuous symmetry, represented by nonrotating ring shaped traps, has attracted renewed theoretical attention in connection with the existence of vortex states, due to recent experimental observations of persistent currents in multiple connected condensates [13, 14]. In particular, by computing the energy landscape, Capuzzi *et al.* [15] have shown that multiply quantized vortices and multivortex configurations can be locally energetically stable in a toroidal trap.

The aim of this work is to study vortex states in a ring-shaped optical lattice with variable barrier heights. This will allow us to explore the transition between the limit of low barrier heights, where large persistent currents are expected, and the high-barrier limit, where Josephson-type links should rule the vortex configurations. For such purpose we will consider a condensate confined by superposition of a toroidal trap and equally spaced radial barriers forming a ring of N_c linked condensates. In particular, we will investigate the energy and angular momentum dependence on the winding number for a wide range of barrier heights. Such a system could be experimentally investigated, as it corresponds to a relatively simple combination of previously implemented experimental settings [9, 14]. Actually, new techniques have been recently developed by Henderson *et al.* [16] to create and manipulate condensates in a variety of geometries, including the present type of ring lattices.

Our work is organized as follows, in Sec. II we describe the theoretical framework utilized to generate stationary states with different winding numbers. Sec. III is devoted to an analytical study of the energy and the angular momentum for limiting values of the barrier height. By numerically solving the Gross-Pitaevskii equation, we calculate in Sec. IV the energy and angular momentum and analyze their dependence on the winding number and the barrier height. Finally, a summary and concluding remarks are offered in Sec. V.

II. THEORETICAL FRAMEWORK

A. The Trap

We consider a Bose-Einstein condensate of Rubidium atoms confined by an external trap V_{trap} , consisting of a superposition of a toroidal term V_{toro} and a lattice potential $V_{\text{L}}(x, y)$ formed by radial barriers. Similarly to the trap utilized in recent experiments [13, 14], the toroidal trapping potential in cylindrical coordinates reads,

$$V_{\text{toro}}(r, z) = \frac{m}{2} [\omega_r^2 r^2 + \omega_z^2 z^2] + V_0 \exp(-2r^2 / \lambda_0^2) \quad (1)$$

where ω_r and ω_z denote the radial and axial frequencies, respectively. We have set $\omega_z \gg \omega_r$ to suppress excitation in the z direction. In particular, we have chosen $\omega_r/(2\pi) = 7.8$ Hz and $\omega_z/(2\pi) = 173$ Hz, while for the laser beam we have set $V_0 = 100 \hbar\omega_r$ and $\lambda_0 = 6 l_r$, with $l_r = \sqrt{\hbar/(m\omega_r)}$. On the other hand, the lattice potential formed by N_c Gaussian barriers located at equally spaced angular positions $\theta_i = 2\pi i/N_c$ ($0 \leq i \leq N_c - 1$) may be written,

$$V_{\text{L}}(x, y) = V_b \sum_{i=0}^{N_c/2-1} \exp \left\{ -\frac{[\cos(\theta_i) y - \sin(\theta_i) x]^2}{\lambda_b^2} \right\} \quad (2)$$

for N_c even. Although, for simplicity the numerical simulations of this work have been restricted to the case of an even number of lattice sites, most of our findings can be easily shown to be valid irrespective of the parity of N_c . We have fixed the trap parameters at $\lambda_b = 0.5 l_r$ and $N_c = 16$. The combination of these potentials gives rise to effective barriers between neighboring sites, as represented in Fig. 1.

The Thomas-Fermi (TF) approximation, will allow us to deduce some general features of the condensate from the characteristics of the trapping potential. To this aim, we will take into account that the TF-density vanishes at points fulfilling $\mu < V_{\text{trap}}(x, y)$, μ being the chemical potential. On the one hand, around the trap center we can approximate $V_{\text{trap}} \simeq V_0 + (N_c/2)V_b$ and, as we restrict our calculations to chemical potentials smaller than V_0 , the condensate center will always exhibit a hole. On the other hand, between neighboring sites we have that the potential minimum shown in the right panel of Fig. 1, which corresponds to the saddle point in two dimensions, turns out to be located around $x_{\text{min}} = 6.6 l_r$, and the barrier height can be approximated as $V_{\text{min}} \simeq V_{\text{trap}}(6.6, 0) = 30.7 \hbar\omega_r + V_b$. Notice that we have retained in this estimate only the $i = 0$ term of the sum in $V_{\text{L}}(x, y)$, as the exponent of

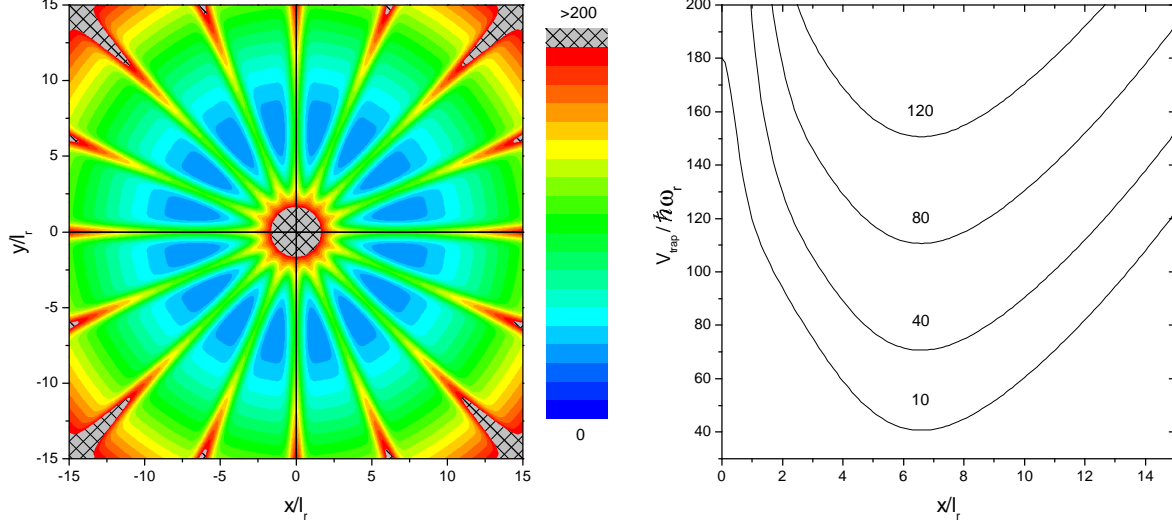


FIG. 1: (Color online) Left panel: equipotential curves for the external trap $V_{\text{trap}}(x, y)/\hbar\omega_r$ with $V_b/\hbar\omega_r = 80$. Right panel: effective potential barrier $V_{\text{trap}}(x, 0)$ along the positive x axis for several values of the parameter $V_b/\hbar\omega_r$.

such a term vanishes, while the contributions of the remaining Gaussian terms are negligible. Thus, when the chemical potential becomes smaller than this potential minimum, the TF-density between neighboring sites vanishes.

B. Stationary States

Since the trapping potential is much stronger along the z axis, the motion of the particles in the z direction remains frozen in the ground state, and the energy per particle in the condensate is then given by the two-dimensional (2D) energy functional [17]

$$E[\psi] = \int \left(\frac{\hbar^2}{2m} |\nabla \psi|^2 + V_{\text{trap}} |\psi|^2 + \frac{1}{2} N g |\psi|^4 \right) dx dy, \quad (3)$$

where $\psi = e^{i\phi}|\psi|$ denotes the 2D order parameter, N the number of particles, and m the atom mass. The effective 2D coupling constant $g = g_{3D}\sqrt{m\omega_z/2\pi\hbar}$ is written in terms of the 3D coupling constant between the atoms $g_{3D} = 4\pi a\hbar^2/m$, where $a = 98.98 a_0$ denotes the s -wave scattering length of ^{87}Rb , a_0 being the Bohr radius. In order to obtain stationary states, one has to perform variations of E with respect to ψ keeping the number of particles

fixed, which yields the Gross-Pitaevskii (GP) equation [18]

$$\left(-\frac{\hbar^2 \nabla^2}{2m} + V_{\text{trap}} + Ng|\psi|^2\right)\psi = \mu\psi. \quad (4)$$

The ground state wavefunction is numerically obtained without imposing any constraint. Typical configurations are shown in Fig. 2, where we depict the equidensity curves for different barrier heights. The left panel corresponds to the barrier-free system, while the middle and right panels correspond to barrier parameters fixed at $V_b/\hbar\omega_r = 10$ and $V_b/\hbar\omega_r = 80$, respectively. We note that the chemical potential verifies $\mu \simeq 77 \hbar\omega_r > V_{\text{min}}$ for the lower barrier, while the higher barrier verifies the opposite inequality $\mu \simeq 90 \hbar\omega_r < V_{\text{min}}$. Thus, as we have explained in the previous section, the TF-density between neighboring sites should vanish in the latter configuration, while remaining finite in the former one. As regards the exact density, it should exhibit a similar behavior, except for a smoother decay.

On the other hand, further constraints must be imposed in order to obtain stationary states with nonvanishing winding numbers, and to this aim we have employed a method which was described in detail in a previous work [19]. Summarizing, we begin by using the ground state wavefunction ψ_0 to construct an initial order parameter with vorticity [15]:

$$\psi(\mathbf{r}) = \psi_0(\mathbf{r}) \left(\frac{x + iy}{\sqrt{x^2 + y^2}}\right)^n, \quad (5)$$

where n denotes the initial winding number or topological charge. From this ansatz, it is straightforward to realize that ψ and ψ_0 possess the same density profile, but ψ presents an imprinted velocity field. Such a field is irrotational everywhere, except at the origin, with a circulation along any closed loop around this point, which must be proportional to the winding number n . Next, we apply a minimizing procedure in order to obtain a stationary state. During the minimization such a velocity field undergoes drastic changes when large barrier heights are considered. Notice that the presence of radial barriers destroys the axial symmetry, and thus the angular momentum does no longer commute with the Hamiltonian. As a consequence, there is also no longer a linear relationship between the value of the angular momentum and the imprinted winding number. In addition, the final winding number n' after the minimization process may differ from the initial one n , as will be shown in Sec. IV, where we will also see that $|n'|$ is bounded by a maximum value, which we shall call ν .

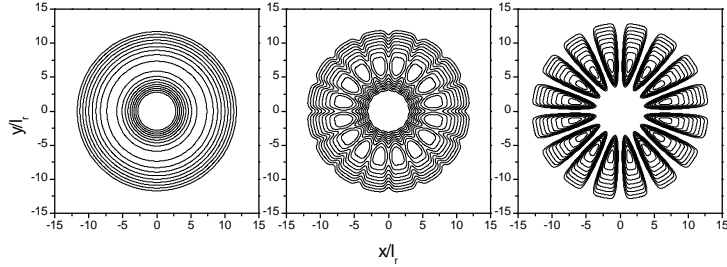


FIG. 2: Density isocontours for several values of the barrier parameter. From left to right: $V_b/\hbar\omega_r = 0, 10$, and 80 . The number of particles corresponds to $N = 10^5$.

III. ANALYTICAL EXPRESSIONS

In this Section, we shall analyze the behavior of the angular momentum and the energy as functions of the winding number in two limiting cases, namely in the absence of barriers and for large barrier heights. In both cases we will derive analytical expressions for the mean values of such observables in terms of ground state magnitudes. Hereafter, when referring to energy and angular momentum, it must be understood that they denote the mean value of the corresponding observables per particle.

A. Barrier free system

Taking into account that the ground state density exhibits a hole at the condensate center, for vanishing barriers and an arbitrary winding number n , the order parameter may be approximated as:

$$\psi_n(r, \theta) = \psi_0(r) e^{in\theta}, \quad (6)$$

where we have assumed that the presence of a non-homogeneous phase in the wavefunction with its concomitant velocity field, does not affect appreciably the shape of the condensate density, as compared to that of the ground state. This occurs because the centrifugal force should have little effect outside the central hole, where the density is non-negligible.

Replacing the wavefunction (6) in the first term of the integrand of (3) we have:

$$\frac{\hbar^2}{2m} |\nabla \psi_n|^2 = \frac{\hbar^2}{2m} (\nabla \psi_0)^2 + \frac{\hbar^2}{2m} (\psi_0)^2 \frac{n^2}{r^2} \quad (7)$$

and one can easily obtain the mean value of the energy as a quadratic function of the winding number n ,

$$E(n) = Kn^2 + E_0 \quad (8)$$

where E_0 denotes the ground state energy and K is given by:

$$K = \frac{\hbar^2}{2m} 2\pi \int \frac{1}{r^2} [\psi_0(r)]^2 r dr. \quad (9)$$

On the other hand, since the angular momentum commutes with the Hamiltonian and the wavefunctions (6) are eigenfunctions of \hat{L}_z , we have the linear relationship

$$L_z = \hbar n. \quad (10)$$

B. High barriers

According to Refs. [12] and [11] the most general solution of the GP equation is a Bloch state of the form:

$$\psi_n(r, \theta) = e^{in\theta} f_n(r, \theta), \quad (11)$$

where the function $f_n(r, \theta)$ is invariant under a $2\pi/N_c$ rotation in θ . This type of solution is valid irrespective of the barrier height. The above periodicity is obvious in the modulus, since $|f_n(r, \theta)|^2 = |\psi_n(r, \theta)|^2$ corresponds to the periodic particle density as shown in Fig. 2. However, the phase of $\psi_n(r, \theta)$ does not necessarily present this symmetry. As an example, in Fig. 3 we depict the phase of $\psi_4(r_0, \theta)$ as a function of the angular coordinate, which clearly does not exhibit such a symmetry. Whereas, it is easy to verify that the phase of $f_4(r_0, \theta) = e^{-i4\theta} \psi_4(r_0, \theta)$ is indeed a $2\pi/N_c$ periodic function.

In this section we will concentrate ourselves on large barrier heights. In such a limit, the phase turns out to be almost uniform in each site, as it may be seen from the right panel of Fig. 3. This is a consequence of the fact that for high barriers, the condensate portions become more isolated and thus the particle current diminishes. This, in turn, implies that the velocity field \vec{v} and hence the gradient of the phase $(m/\hbar)\vec{v}$ practically vanishes within each portion. Then, for large enough barriers, such that the chemical potential verifies $\mu < V_{min}$,

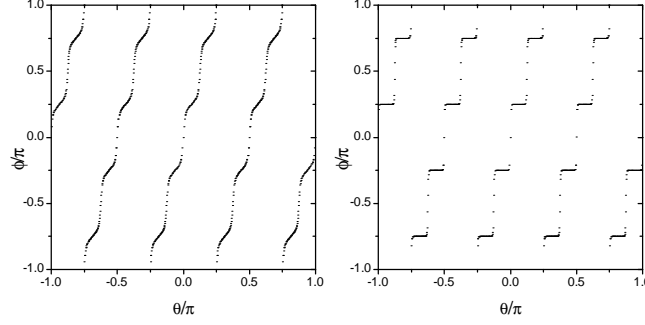


FIG. 3: Phase of the order parameter ϕ as a function of the angular coordinate for $r_0 = 6l_r$, a winding number $n = 4$, and two values of the barrier height $V_b/\hbar\omega_r = 60$ (left panel) and $V_b/\hbar\omega_r = 120$ (right panel). The number of particles is $N = 10^5$.

the system splits into a ring of weakly linked condensates, and the order parameter can be approximated as follows,

$$\psi_n(r, \theta) = \sum_{k=0}^{N_c-1} \Psi_k(r, \theta) e^{i2\pi nk/N_c}, \quad (12)$$

where $\Psi_k(r, \theta)$ is a real function describing a localized state in the k -site, i.e., having only a very little overlap with neighboring sites. This approximation is analogous to the tight-binding approximation [21], and the matrix element $\psi_n^* \hat{\mathcal{O}} \psi_n$ of a given observable $\hat{\mathcal{O}}$ can be approximated as

$$\sum_{k=0}^{N_c-1} \Psi_k \hat{\mathcal{O}} \Psi_k + e^{i\frac{2\pi n}{N_c}} \sum_{k=0}^{N_c-1} \Psi_k \hat{\mathcal{O}} \Psi_{k+1} + e^{-i\frac{2\pi n}{N_c}} \sum_{k=0}^{N_c-1} \Psi_k \hat{\mathcal{O}} \Psi_{k-1}, \quad (13)$$

where we have assumed that only the matrix elements between neighboring sites are non-negligible. In our notation, the site denoted by $k = N_c$ ($k = -1$) is identified with that of $k = 0$ ($k = N_c - 1$). Then, as the summation is performed over all k values, we can rewrite the expression (13) as follows:

$$\sum_{k=0}^{N_c-1} \Psi_k \hat{\mathcal{O}} \Psi_k + e^{i\frac{2\pi n}{N_c}} \sum_{k=0}^{N_c-1} \Psi_k \hat{\mathcal{O}} \Psi_{k+1} + e^{-i\frac{2\pi n}{N_c}} \sum_{k=0}^{N_c-1} \Psi_{k+1} \hat{\mathcal{O}} \Psi_k. \quad (14)$$

Let us now assume that the observable $\hat{\mathcal{O}}$ is the angular momentum operator:

$$\hat{\mathcal{O}} = \hat{L}_z = \frac{\hbar}{i} \frac{\partial}{\partial \theta}. \quad (15)$$

Using that \hat{L}_z is hermitian and Ψ_k are real functions, the following equalities hold:

$$\Psi_k \hat{L}_z \Psi_k = 0 \quad (16)$$

$$\Psi_k \hat{L}_z \Psi_{k+1} = -\Psi_{k+1} \hat{L}_z \Psi_k \quad (17)$$

Then replacing (16) and (17) in (14) we obtain

$$\psi_n^* \hat{L}_z \psi_n = \frac{\hbar}{i} (e^{i\frac{2\pi n}{N_c}} - e^{-i\frac{2\pi n}{N_c}}) \sum_{k=0}^{N_c-1} \Psi_k \frac{\partial \Psi_{k+1}}{\partial \theta} \quad (18)$$

and thus the mean value of the angular momentum reads:

$$\int \psi_n^* \hat{L}_z \psi_n r dr d\theta = 2 \hbar \sin(2\pi n/N_c) \sum_{k=0}^{N_c-1} \int \Psi_k \frac{\partial \Psi_{k+1}}{\partial \theta} r dr d\theta. \quad (19)$$

Note in the above expression that the winding number appears only in the argument of the sine, which determines that the angular momentum must exhibit a sinusoidal behavior as a function of n .

In computing the mean value of the energy, it is convenient to separately treat the interacting and noninteracting terms. In fact, the noninteracting part, which corresponds to the observable $\hat{\mathcal{O}}_s = -\frac{\hbar^2 \nabla^2}{2m} + V_{\text{trap}}$, may be treated analogously to the angular momentum, yielding

$$\Psi_k \hat{\mathcal{O}}_s \Psi_{k+1} = \Psi_{k+1} \hat{\mathcal{O}}_s \Psi_k, \quad (20)$$

which replaced in (14) leads to

$$\begin{aligned} \int \int \psi_n^* \hat{\mathcal{O}}_s \psi_n r dr d\theta &= \sum_{k=0}^{N_c-1} \int \int \Psi_k \hat{\mathcal{O}}_s \Psi_k r dr d\theta \\ + 2 \cos(2\pi n/N_c) \sum_{k=0}^{N_c-1} \int \int \Psi_k \hat{\mathcal{O}}_s \Psi_{k+1} r dr d\theta. \end{aligned} \quad (21)$$

On the other hand, the interacting term corresponds to the nonlinear operator $\hat{\mathcal{O}}_{nl} = \frac{g}{2} N |\psi_n|^2$, proportional to the particle density, for which the approximation (14) is no longer valid. In this case, the mean value must be computed to first order in the product of adjacent wavefunctions $\Psi_k \Psi_{k+1}$, yielding

$$\frac{g}{2} N \int \int |\psi_n|^4 r dr d\theta = \sum_{k=0}^{N_c-1} \int \int \frac{g}{2} N \Psi_k^4 r dr d\theta$$

$$+ 2 g N \cos(2\pi n/N_c) \sum_{k=0}^{N_c-1} \int \int (\Psi_k^3 \Psi_{k+1} + \Psi_k \Psi_{k+1}^3) r dr d\theta. \quad (22)$$

Finally, from (21) and (22) we may conclude that the mean value of the energy will present a dependence of the type $\cos(2\pi n/N_c)$ on the winding number.

IV. ENERGY AND ANGULAR MOMENTUM: NUMERICAL RESULTS

A. Low barriers

A vanishing barrier ($V_b = 0$) yields a ground state chemical potential $\mu = 33.19 \hbar \omega_r$ ($\mu = 73.31 \hbar \omega_r$) for $N = 10^3$ ($N = 10^5$) particles. Such values turn out to be smaller than V_0 , and thus, as discussed in Section II, the corresponding condensates exhibit a hole at their centers [20]. It has been shown, both experimentally [13] and theoretically [15], that this type of configuration forming a torus can host locally stable multiply quantized vortices. We have found such stable vortices up to a maximum winding number of $\nu = 7$ ($\nu = 9$) for $N = 10^3$ ($N = 10^5$), reflecting the fact that ν depends on the number of particles. Actually, we will next see that ν also depends on the barrier height.

In the top panel of Figs. 4 and 5 we depict the excitation energy $E'_n = E(n) - E_0$ as a function of the winding number. In the case of a vanishing barrier, we have also numerically evaluated the parameter K of Eq. (9), obtaining the values 0.01156 and 0.01114 for $N = 10^3$ and $N = 10^5$, respectively. Thus, we have drawn the curve arising from formulae (8), which shows an excellent agreement with the numerically obtained values (circles), as seen from Figs. 4 and 5. It may also be observed that the energy decreases for increasing values of the barrier height, retaining, however, the approximately quadratic behavior predicted by Eq. (8).

The bottom panel of Figs. 4 and 5 shows the angular momentum as a function of the winding number. Note that for a vanishing barrier, the numerical results correspond to the straight line predicted by Eq. (10), while we may observe that the angular momentum decreases and curves down for increasing values of the barrier height. In the same sequence, we may also observe a decreasing value of the maximum winding number ν the system can host. In fact, we have found that for a given barrier height, the time evolution with a moderate dissipation [22] of an initial state with winding number $n > \nu$, may lead to

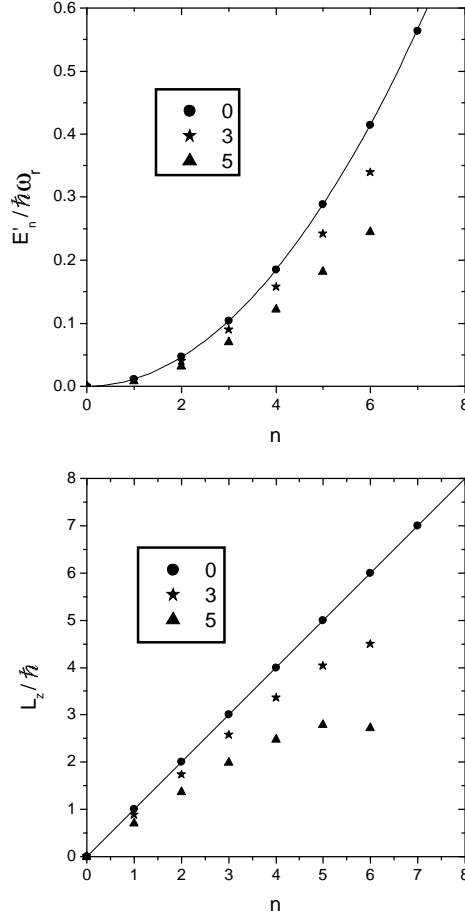


FIG. 4: Excitation energy per particle E'_n (top panel), and angular momentum per particle $L_z = \langle \hat{L}_z \rangle$ (bottom panel), as functions of the winding number for $N = 10^3$ particles and $V_b/\hbar\omega_r = 0$ (circles), 3 (stars), and 5 (triangles). The solid lines correspond to Eq. (8) (top) and Eq. (10) (bottom).

different processes of vorticity reduction, which involve vortex motion along the barriers. Such a vortex dynamics may either simply consist of a vortex escaping phenomenon or, by contrast, it may contain more complex processes such as, vortex escaping with the aid of antivortices. We describe in the following this last particular process. Fig. 6 shows a series of snapshots in time of the phase distribution when a winding number $n = 9$ is initially imprinted in the condensate of 10^5 particles and barrier height $V_b/\hbar\omega_r = 40$ (panel(a)). We recall that the maximum winding number for this barrier height is $\nu = 7$, as shown in Fig. 5. The time evolution first yields a ring of 16 vortices of topological charge $m = +1$, denoted as white dots in panel (b), which move along the barriers from the condensate center outwards.

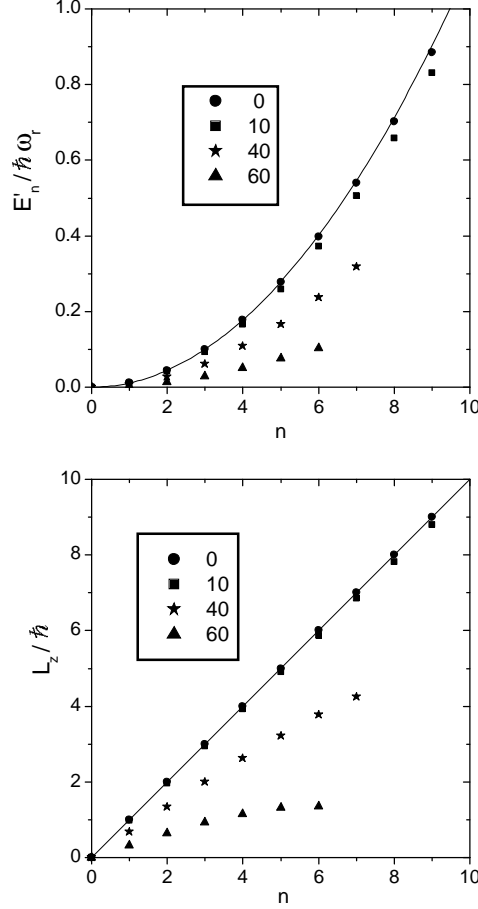


FIG. 5: Same as Fig. 4 for the condensate of $N = 10^5$ particles with barrier heights $V_b / \hbar \omega_r = 0$ (circles), 10 (squares), 40 (stars), and 60 (triangles).

Thus, the circulation along the dashed line circle in panel (b) still bears $n = 9$, while the same calculation for a circle within the vortex ring would yield -7. However, to reach the condensate border, each vortex should overcome the high density region corresponding to the potential minimum shown at the left panel of Fig. 1, which approximately lies around the dashed line circles shown in Fig. 6. Such a displacement would produce an overall increase in energy that is actually avoided by the generation of an outer ring of antivortices, denoted as black dots in panel (c). This leads to the formation of vortex-antivortex pairs, i.e., dipoles, of lower kinetic energy that are then able to keep on moving towards the condensate edge, leaving behind them a pattern of centered vorticity of winding number -7. This process is accompanied by a progressive reduction of the separation of both charges at each dipole. In the last panel (d), we may observe that each dipole is about to annihilate itself, while the

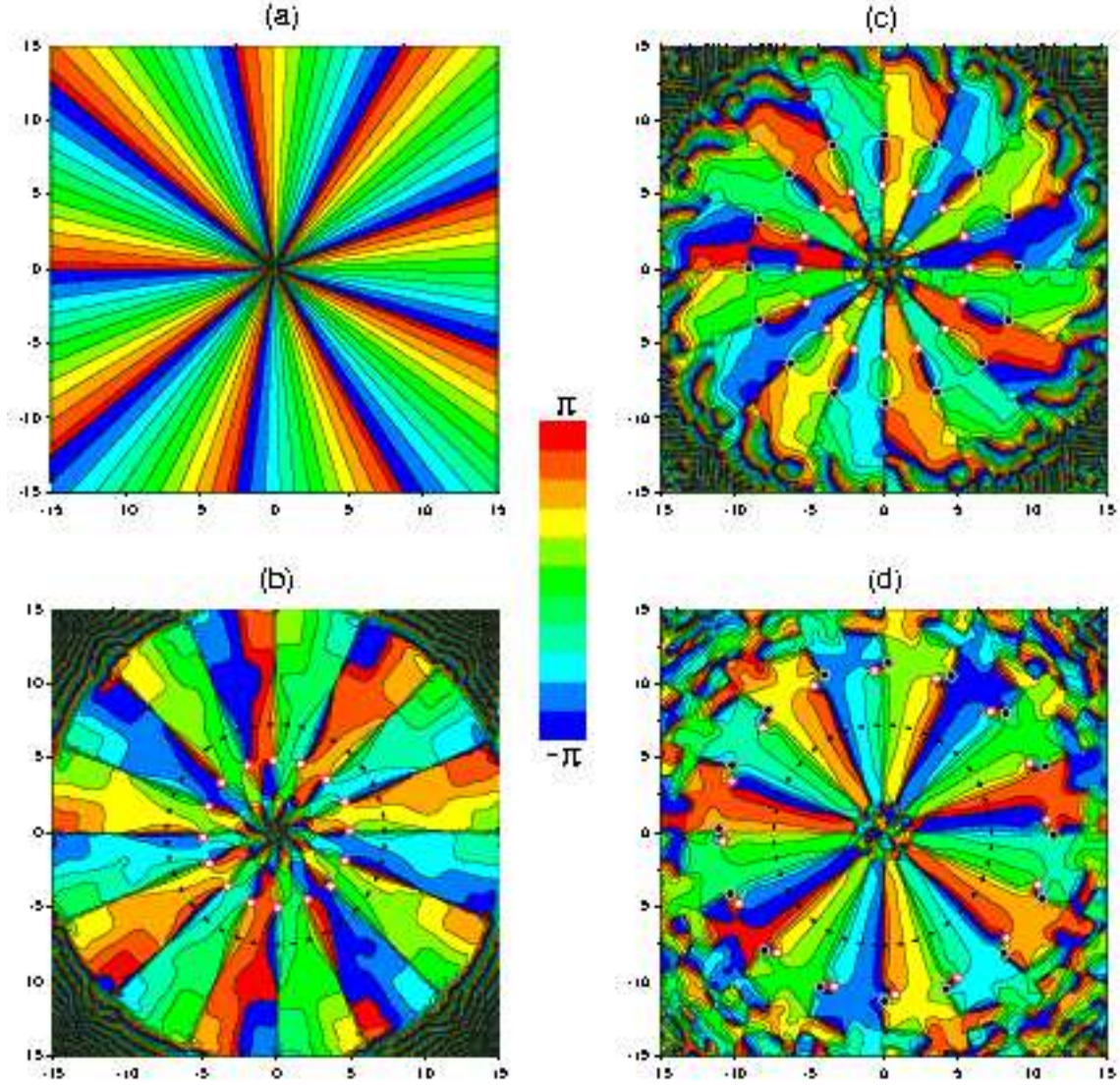


FIG. 6: (Color online) Snapshots of the phase distribution in the condensate of 10^5 particles with a barrier height $V_b/\hbar\omega_r = 40$ and an initially imprinted winding number $n = 9$. Panels (a) to (d) correspond to $\omega_r t = 0, 0.374, 0.796$, and 3.183 , respectively. White dots in panels (b) to (d) denote vortices with topological charge $m = +1$, while black dots in (c) and (d) denote antivortices with $m = -1$. The dashed line circles in (b) and (d) correspond to circulations yielding initial $n = 9$ and final $n' = -7$ winding numbers, respectively.

final $n' = -7$ central vorticity pattern becomes evident by following the circulation along the dashed line circle.

Finally, we want to remark that time evolutions with $n \leq \nu$ always lead to an identical final winding number $n' = n$, with the vorticity concentrated at the central hole.

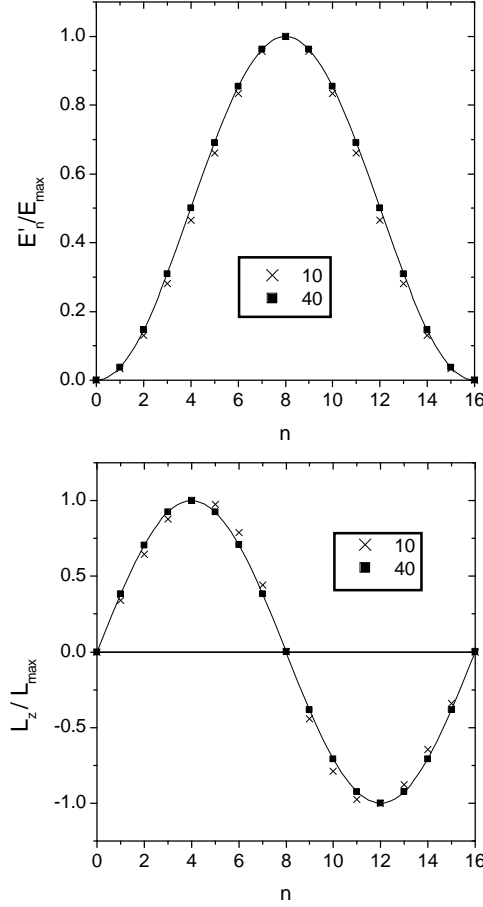


FIG. 7: Excitation energy per particle E'_n (top panel) and angular momentum per particle $L_z = \langle \hat{L}_z \rangle$ (bottom panel), in units of their maximum values E_{\max} and L_{\max} , respectively, as functions of the winding number for the condensate of $N = 10^3$ particles, with barrier heights $V_b/\hbar\omega_r = 10$ (crosses) and 40 (squares). The solid lines represent the functions: $[1 - \cos(2\pi n/N_c)]/2$ (top panel) and $\sin(2\pi n/N_c)$ (bottom panel).

B. High barriers

Now we will study the numerical results obtained for the high-barrier regime which was analytically investigated in Sec. IIIB. We depict in Figs. 7 and 8, the excitation energy (top panel) and the angular momentum (bottom panel), as functions of the winding number for the condensates of 10^3 and 10^5 particles, respectively. We may observe that while both magnitudes are well described by the periodic functions obtained in IIIB, there still exist for the lower barrier heights, $V_b/\hbar\omega_r = 10$ and 80, some noticeable differences between the

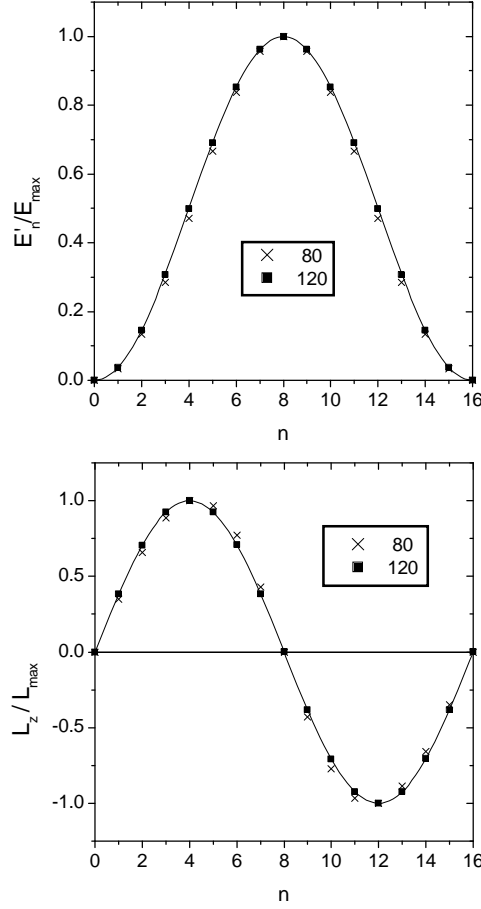


FIG. 8: Same as Fig. 7 for the condensate of $N = 10^5$ particles with barrier heights $V_b/\hbar\omega_r = 80$ (crosses) and 120 (squares).

numerical values and the predicted curves.

Irrespective of the number of particles, we have observed in this regime the processes predicted by Pérez-García *et al.* [11], namely the so-called charge *erasure*, which occurs only for an even number of lattice sites, and charge *inversion*. In fact, for an imprinted winding number $n = N_c/2 = 8$, the phases between neighboring sites differ in π (top panels of Fig. 9), leading to a vanishing net flux of particles, or in other words, to an erasure of vorticity. Notice that such a state presents a vanishing angular momentum and a maximum of energy, as shown in Figs. 7 and 8. On the other hand, charge inversion takes place if $n > N_c/2$, as shown in the bottom panels of Fig. 9. In this case, the phase difference between neighboring sites $\Delta\phi$ becomes larger than π , which amounts to an effective phase difference of $2\pi - \Delta\phi$. Thus, the phase derivative $\partial\phi/\partial\theta$ changes sign, giving rise to an inverted

current density with a corresponding negative angular momentum (see Figs. 7 and 8), and a final winding number $n' = n - N_c$. We have found that repeating the dissipative real-time simulation of Sec. IV A, but for a higher barrier of $V_b/\hbar\omega_r = 80$, leads to vortex escaping along each of the 16 barriers and a final state of vorticity $n' = -7$, localized within the condensate central hole. However, it is interesting to notice that in contrast to the low barrier regime (see Fig. 6), where the vortices may be viewed as point charges, we observe in Fig. 10 a remarkable phenomenon of vorticity spreading of the escaping vortices.

Summarizing, we may realize that there exists in this regime, irrespective of the number of particles, $N_c = 16$ different stationary states, namely $N_c - 2 = 14$ ‘multivortex’ states corresponding to final winding numbers $1 \leq |n'| \leq N_c/2 - 1 = 7$, plus a single excited state of maximum energy and vanishing particle current corresponding to $n = N_c/2 = 8$, and the ground state ($n = 0$). These results are valid for any even number of lattice sites. For an odd number of sites, on the other hand, the only difference would be given by the absence of the single excited state of maximum energy and vanishing angular momentum, i.e., we would have $N_c - 1$ ‘multivortex’ states corresponding to final winding numbers $1 \leq |n'| \leq (N_c - 1)/2$, apart from the ground state with $n = 0$ [11, 12].

Finally, in Fig. 11 we depict the chemical potential of the ground state as a function of the barrier height V_b , jointly with the effective potential barrier minima V_{min} shown in Fig. 1. We notice that V_{min} approximately intersects the chemical potentials corresponding to 10^3 and 10^5 particles at $V_b = 5 \hbar\omega_r$ and $V_b = 60 \hbar\omega_r$, respectively. Such intersections correspond to transitions between the low- and high-barrier regimes above described, i.e., they indicate the barrier height above which the quantum tunneling regime becomes dominant.

V. SUMMARY AND CONCLUDING REMARKS

We have analyzed the angular momentum and energy as functions of the winding number in a ring-shaped lattice, finding two clearly differentiated regimes, according to the relative value of the barrier height as compared to the chemical potential. On the one hand, we have found that for low barriers, there exists an almost quadratic dependence on the winding number for the energy and a linear dependence for the angular momentum, as it is analytically derived in the absence of barriers. For high barriers, on the other hand, we have found that the energy and the angular momentum turn out to be accurately described by

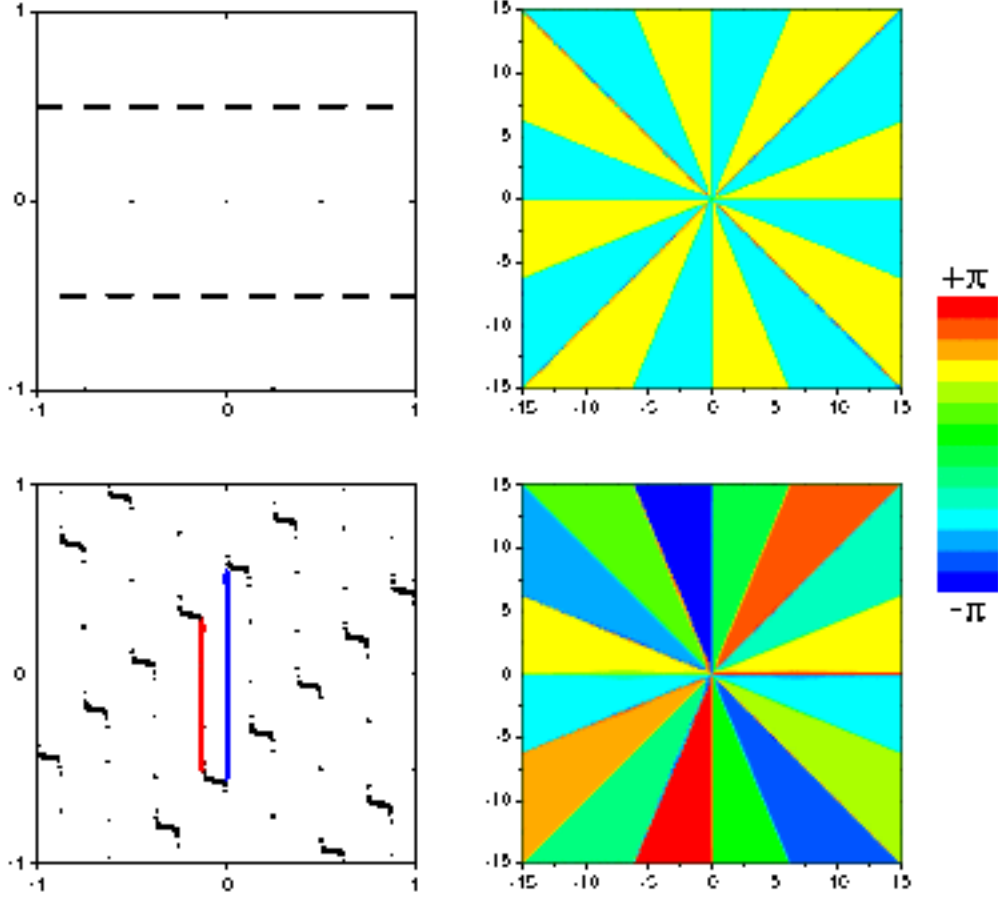


FIG. 9: (Color online) Phase of the order parameter as a function of the angular coordinate (both in units of π) for $r_0 = 6l_r$ (left panels), and phase distribution in the x - y plane (right panels), in the condensate of 10^5 particles with a barrier height $V_b/\hbar\omega_r = 80$. The imprinted winding number is $n = 8$ (top panels) and $n = 9$ (bottom panels). The long (blue) vertical arrow in the left-bottom panel shows a phase difference between neighboring sites larger than π , which amounts to the smaller phase difference denoted by the short (red) arrow. Note also the slightly negative phase slope within each site, $\partial\phi/\partial\theta < 0$, which yields the final winding number $n' = 9 - N_c = -7$ and the corresponding negative angular momentum, as seen in the bottom panel of Fig. 8.

sinusoidal functions, as predicted from a simple analytical model. We have observed these regimes irrespective of the number of particles, and a remarkable difference between them consists in that for the low-barrier regime, metastable vortex states are obtained up to a maximum winding number ν , which depends on the particle number and the barrier height, whereas, for high barriers, such states are obtained up to a maximum winding number which

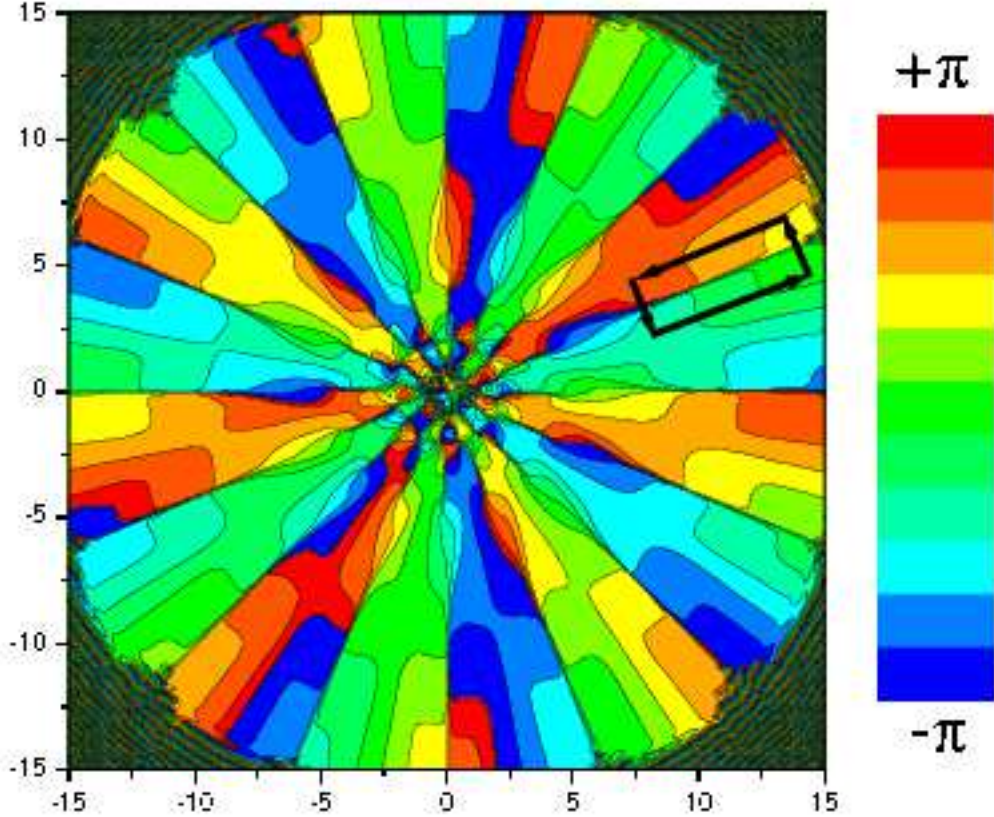


FIG. 10: (Color online) Snapshot of the phase distribution in the condensate of 10^5 particles with a barrier height of $V_b/\hbar\omega_r = 80$ and an initially imprinted winding number $n = 9$. Real-time dissipative evolution at $t = 0.2387\omega_r^{-1}$ showing vorticities with a topological charge $m = +1$ spread along each barrier. Such a spreading may be appreciated by following the circulation along the rectangular contour enclosing one of the barriers.

only depends on the number of lattice sites. Another difference between both regimes stems from the way in which vorticity becomes reduced from an initially imprinted winding number exceeding ν . For a low barrier, this process involves the displacement outwards along the barriers of positive point charges, jointly with an eventual generation of negative charges at the condensate edge. Such antivortices penetrate along the barriers to form dipoles that, by diminishing the energy from velocity field, are then able to cross the maximum density region outwards. On the other hand, the vorticity reduction in the large-barrier regime proceeds through the appearance of stretched positive vorticities along each barrier, which eventually escape from the condensate.

To conclude, we believe that the present study could also be regarded as a first stage

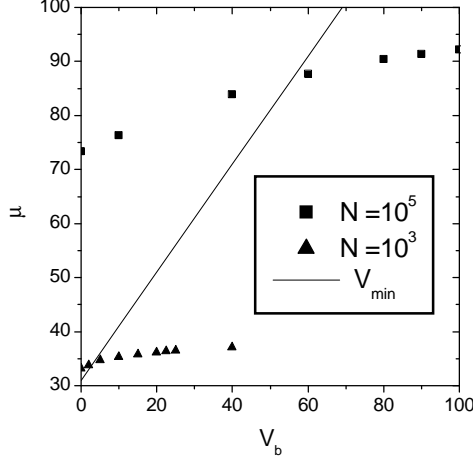


FIG. 11: Ground state chemical potential μ of the condensate containing 10^5 particles (squares) and 10^3 particles (triangles) as a function of the barrier height V_b . The solid line corresponds to the effective potential barrier minima of Fig. 1. All quantities are given in units of $\hbar\omega_r$.

to establish a Bose-Hubbard model for ring-shaped optical lattices with a large occupation number per site.

Acknowledgments

DMJ acknowledges CONICET for financial support under Grant No. PIP 11420090100243.

-
- [1] R. Gati and M. K. Oberthaler, J. Phys. B **40** R61 (2007).
 - [2] M. Asad-uz-Zaman and D. Blume, Phys. Rev. A **80**, 053622 (2009); N. Teichmann, M. Es-
mann, and C. Weiss, Phys. Rev. A **79**, 063620 (2009); D. Witthaut, F. Trimborn, and S.
Wimberger, Phys. Rev. A **79**, 033621 (2009); M. T. Martinez, A. Posazhennikova, and J.
Kroha, Phys. Rev. Lett. **103**, 105302 (2009); B. Juliá-Díaz, D. Dagnino, M. Lewenstein, J.
Martorell, and A. Polls, Rev. A **81**, 023615 (2010).
 - [3] I. Zapata, F. Sols, and A. J. Leggett, Phys. Rev. A **57**, 28 (1998).
 - [4] I. Zapata, F. Sols, and A. J. Leggett, Phys. Rev. A **67**, 021603 (2003).
 - [5] A. Smerzi, S. Fantoni, S. Giovanazzi, and S. R. Shenoy, Phys. Rev. Lett. **79**, 4950 (1997).

- [6] S. Raghavan, A. Smerzi, S. Fantoni, and S. R. Shenoy, Phys. Rev. A **59**, 620 (1999).
- [7] D. Ananikian and T. Bergeman, Phys. Rev. A **73**, 013604 (2006).
- [8] M. Albiez, R. Gati, J. Fölling, S. Hunsmann, M. Cristiani, and M. K. Oberthaler, Phys. Rev. Lett. **95**, 010402 (2005).
- [9] D. R. Scherer, C. N. Weiler, T. W. Neely, and B. P. Anderson, Phys. Rev. Lett. **98**, 110402 (2007).
- [10] P. Ghosh and F. Sols, Phys. Rev. A **77**, 033609 (2008).
- [11] V. M. Pérez-García, M. A. García-March, and A. Ferrando, Phys. Rev. A **75**, 033618 (2007).
- [12] A. Ferrando, Phys. Rev. E **72**, 036612 (2005).
- [13] C. Ryu, M. F. Andersen, P. Cladé, Vasant Natarajan, K. Helmerson, and W. D. Phillips, Phys. Rev. Lett. **99**, 260401 (2007).
- [14] C. N. Weiler, T. W. Neely, D. R. Scherer, A. S. Bradley, M. J. Davis, and B. P. Anderson, Nature **455**, 948 (2008).
- [15] P. Capuzzi and D. M. Jezek, J. Phys. B **42**, 145301 (2009).
- [16] K. Henderson, C. Ryu, C. MacCormick, and M. G. Boshier, New J. Phys. **11**, 043030 (2009).
- [17] Y. Castin and R. Dum, Eur. Phys. J. D **7**, 399 (1999).
- [18] E. P. Gross, Nuovo Cimento **20**, 454 (1961); L. P. Pitaevskii, Zh. Eksp. Teor. Fiz. **40**, 646 (1961) [Sov. Phys. JETP **13**, 451 (1961)].
- [19] D. M. Jezek, P. Capuzzi, and H. M. Cataldo, J. Phys. B **41**, 045304 (2008).
- [20] H. M. Cataldo and D. M. Jezek, Eur. Phys. J. D **54**, 585 (2009).
- [21] N. W. Ashcroft and N. D. Mermin, *Solid State Physics*, (Saunders College Publishing, Fort Worth, 1976), chap. 10.
- [22] We have employed a phenomenological damped GP equation (see, e.g., K. Kasamatsu, M. Tsubota, and M. Ueda, Phys. Rev. A **67**, 033610 (2003)) with a damping coefficient $\gamma = 0.03$.